PCCP

PAPER

View Article Online
View Journal | View Issue

Cite this: *Phys. Chem. Chem. Phys.*, 2021, **23**, 18525

Ultrafast vibrational wave packet dynamics of the aqueous tyrosyl radical anion induced by photodetachment†

Muhammad Shafiq Bin Mohd Yusof, Yong Liang Lim and Zhi-Heng Loh *

The ultrafast dynamics triggered by the photodetachment of the tyrosinate dianion in aqueous environment shed light on the elementary processes that accompany the interaction of ionizing radiation with biological matter. Photodetachment of the tryosinate dianion yields the tyrosyl radical anion, an important intermediate in biological redox reactions, although the study of its ultrafast dynamics is limited. Here, we utilize femtosecond optical pump–probe spectroscopy to investigate the ultrafast structural reorganization dynamics that follow the photodetachment of the tyrosinate dianion in aqueous solution. Photodetachment of the tyrosinate dianion leads to vibrational wave packet motion along seven vibrational modes that are coupled to the photodetachment process. The vibrational modes are assigned with the aid of density functional theory (DFT) calculations. Our results offer a glimpse of the elementary dynamics of ionized biomolecules and suggest the possibility of extending this approach to investigate the ionization-induced structural rearrangement of other aromatic amino acids and larger biomolecules.

Received 1st July 2021,
Accepted 15th August 2021

DOI: 10.1039/d1cp02975d

rsc.li/pccp

Introduction

The photoionization of biomolecules in aqueous system involves the interaction of high-energy radiation with biological matter to yield the corresponding radical species and the hydrated electron. The formation of these reactive species in turn triggers a plethora of chemical reactions that form the basis of radiation chemistry and radiation biology.[1–3] The investigation of radiation damage involving redox-active amino acids, such as tyrosine, tryptophan, and phenylalanine, is particularly pertinent due to their facile oxidation, which is in turn afforded by their relatively low ionization potentials. In the gas phase, the vertical ionization energies of redox-active amino acids are ~1–2 eV lower than those with aliphatic side chains.[4,5] In aqueous solution, the lowest vertical ionization energies of tyrosine, tryptophan, and phenylalanine have been measured to be 7.8 eV, 7.3 eV, and 8.8 eV, respectively.[6] These vertical ionization energies are downshifted by ~0.6–0.7 eV relative to the gas-phase values due to the stabilization of the radical cation final state by the polar solvent environment.

In this study, we focus on tyrosine (Tyr), an amino acid with a phenolic side chain. Tyrosine participates in biological activities such as protein phosphorylation,[7–10] DNA repair,[11–14] and photoreception.[15] A key intermediate in many of these processes is the tyrosyl radical ($\mathrm{Tyr}^{\bullet}$), whose involvement in proton-coupled electron transfer (PCET) has been the subject of extensive experimental and theoretical studies.[11,13–19] Early microsecond flash photolysis and nanosecond laser experiments have elucidated the formation of the tyrosyl radical *via* the triplet state of tyrosine and its subsequent bimolecular reactions.[20–22] Ultraviolet resonance Raman[23,24] and FTIR spectroscopies[25] have identified the characteristic vibrational frequencies of the tyrosyl radical, both in aqueous solution and in a peptide matrix.[26–28]

While numerous studies have unraveled the dynamics of the hydrated electron produced by the photoionization of aqueous solutes,[29–35] investigations of the ultrafast dynamics of the accompanying radical species are relatively limited. Here, building upon our earlier work on the photodetachment of aqueous phenoxide,[36] we aim to elucidate the ultrafast vibrational wave packet dynamics of the tyrosyl radical anion ($\mathrm{Tyr}^{\bullet -}$) triggered by the photodetachment of the tyrosinate dianion (Tyr^{2-}; Fig. 1) in aqueous solution. When driven by an ultrashort laser pulse, photodetachment triggers ultrafast vibrational wave packet dynamics involving vibrational modes along which the equilibrium geometries before and after electron ejection are displaced.[36] Vibrational modes that appear in the wave packet dynamics therefore encode structural reorganization. In our experiment, vibrational coherences will be detected by near-ultraviolet transient absorption spectroscopy, performed with ~10 fs time resolution. This time-domain approach complements

---

Division of Chemistry and Biological Chemistry, School of Physical and Mathematical Sciences, Nanyang Technological University, 21 Nanyang Link, Singapore 637371, Singapore. E-mail: zhiheng@ntu.edu.sg

† Electronic supplementary information (ESI) available. See DOI: 10.1039/d1cp02975d

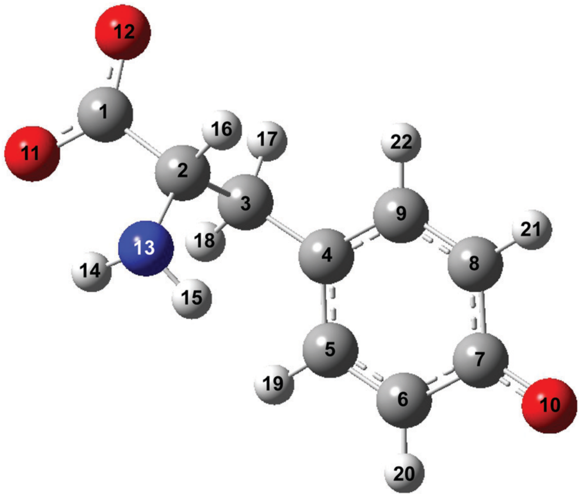

Fig. 1 Structure of the tyrosinate dianion (Tyr^{2-}). The carbon, hydrogen, oxygen and nitrogen atoms are in gray, white, red and blue, respectively.

energy-resolved measurements of the Franck–Condon progression by photoelectron spectroscopy. For amino acids in aqueous solution, however, their Franck–Condon progression is obfuscated by the ~1 eV-wide, inhomogeneously broadened valence photoelectron bands.[6]

Aside from its relevance to radiation chemistry and biological redox reactions, the choice of the tyrosine for the present study is also motivated by several practical considerations. First, the estimated vertical ionization energy of the tyrosinate dianion (~7.1 eV)[6,37] is lower compared to those of liquid water (11.2 eV)[38–41] and aqueous hydroxide (9.2 eV).[42] When driving photodetachment in the strong-field limit, the lower vertical ionization energy of the tyrosinate dianion favors its photodetachment and minimizes contributions from the photodetachment of aqueous hydroxide and the solvent to the transient absorption signal. Second, the dianion form is more water-soluble (60.0 mM at pH 13) than the neutral form (2.7 mM at isoelectronic point),[43] hence further increasing the contribution from the photodetachment of tyrosinate to the transient absorption signal. Third, the absorption signature of the tyrosyl radical at ~400 nm[22,44,45] is located away from the strong absorption peak of the hydrated electron byproduct at ~720 nm,[46] thus enabling a clear view of the tyrosyl radical absorption spectrum evolving in time due to vibrational wave packet motion.

Here, we present the ultrafast vibrational wave packet dynamics induced by the photodetachment of the tyrosinate dianion in aqueous solution. We identify the vibrational modes of the tyrosyl radical anion along which structural reorganization occurs upon photodetachment. Our experimental results are complemented by DFT calculations of vibrational frequencies of the aqueous tyrosyl radical anion. This study provides further insights into the ultrafast structural dynamics that accompany the interaction ionization radiation with biological matter.

Methods

Experimental

The experimental procedure has been described previously.[36] A chirped-pulse-amplified Ti:sapphire laser system (Coherent, Legend Elite Duo-USX) is used to perform the photodetachment of tyrosinate anion. The laser system produces 4.5 mJ, 30 fs pulses at 1 kHz repetition rate and 800 nm center wavelength. The pulses undergo self-phase modulation in a helium-filled hollow-core fiber before they are temporally compressed by chirped mirrors (Ultrafast Innovations GmbH, PC1332). The compressed pulses are incident on a beam splitter (Layertec, 131191), with 80% of the transmitted beam (~0.6 mJ) being directed to a 4*f* visible-NIR pulse shaper equipped with a 128-element spatial light modulator (SLM) (Biophotonics Solutions, FemtoJock-P). The pulse shaper performs adaptive pulse compression of the visible-NIR beam to correct for any higher-order dispersion introduced by the various optical components in the laser beams path to ensure that clean, transform-limited pulses are produced for the experiment. The fundamental spectrum of the visible-NIR beam is truncated to a wavelength range of 520 nm to 750 nm, with a central wavelength of 630 nm (1.97 eV photon energy; Fig. S1, ESI†). Transform-limited laser pulses with full-width half-maximum (FWHM) duration of 5.2 fs are obtained by using multiphoton intrapulse interference phase scan (MIIPS) to measure the spectral phase at the sample, followed by using the SLM to introduce an oppositely signed phase to the laser pulse, thus compressing it to the transform-limited duration.[47] Subsequently, an interferometric autocorrelation trace is recorded by multiple independent comb shaping (MICS) (Fig. S2, ESI†).[48]

The transform-limited pulses, which function as the strong-field ionizing pump, are directed to the sample. The ionizing pump pulses are focused onto the sample by a 50 cm focal length concave mirror. The beam waist (1/e^2 radius) of the pump at the sample target is 120 μm. A maximum pulse energy of 25 μJ is directed to the tyrosine solution, yielding a peak intensity of 2.0×10^{13} W cm^{-2}. An optical delay stage line, driven by a piezo translation stage (Physik Instrumente, N-664.3A), is positioned in the ionizing pump beam path to provide a variable time delay between pump and probe pulses in 5 fs steps.

The remaining output from the chirped mirror compressor passes through a pair of wedges (Femtolasers, OA124), follow by a 50 μm-thick Type 1 beta-barium borate (BBO) crystal (Casix, $\theta = 29.0°$) to generate the UV probe *via* second harmonic generation. The broadband UV probe spans 360 nm to 460 nm (Fig. S1(b), ESI†). A pair of dichroic beamsplitters (Layertec, 109433) placed after the BBO crystal removes the residual fundamental beam. The UV beam is then split off by a reflective neutral density filter (Newport, FRQ-ND05) to produce the probe and reference pulses. The reflected UV probe is focused onto the sample by a 15 cm focal-length off-axis parabolic reflector (Thorlabs). The focused UV probe at the sample target has a beam waist (1/e^2 radius) of 42 μm and a pulse energy of 17 nJ. The peak intensity of the UV probe is 5.2×10^{10} W cm^{-2}.

A slit nozzle (Metaheuristics, Type L) is used in conjunction with a peristaltic pump (Cole-Parmer, 07528-10) and a pulse dampener to produce a microjet of the tyrosinate dianion solution for experiments. The volume flow rate of 92 mL min^{-1} translates to a vertical flow rate of approximately 8.5 mm ms^{-1}, sufficiently high to ensure that a fresh volume of the tyrosinate dianion solution is exposed to each ionizing pump pulse. A liquid jet of 7 μm thickness is produced, which yields a sizeable differential absorption signal ($\Delta A \sim 0.1$), while minimizing the temporal broadening of the pulses in the liquid jet due to dispersion. In addition, a thin liquid jet limits the group-velocity mismatch between the pump and probe to <1 fs, making its effect on the time resolution negligible.

A synchronized optical chopper is placed in the ionizing pump beam path before the sample to modulate the repetition rate of the ionizing pump at 0.5 kHz. The probe beam that is transmitted through the microjet is focused into a 300 mm spectrograph (Princeton Instruments, Acton SP2300). The spectrograph is equipped with a 600 grooves per mm grating blazed at 500 nm and a 1024-pixel silicon (Si) photodiode array detector (Stresing, S8381-1024Q) with a read-out rate of 1 kHz, which allows simultaneous acquisition of probe spectra obtained with and without the ionizing pump pulse. The reference UV pulses are focused into an identical spectrograph, which is equipped with a similar grating and photodiode array operating at 1 kHz repetition rate. Referenced detection reduces noise caused by shot-to-shot fluctuations of the probe beam. The Si photodiode array detectors are interfaced to desktop computers for automated data acquisition.

L-Tyrosine (Sigma-Aldrich, ≥98% HPLC) and sodium hydroxide (VWR Chemicals, 98.9% pellets) are used as received. Since L-tyrosine has relatively low solubility in water (2.7 mM at its isoelectronic point),[43] L-tyrosine is dissolved and sonicated in sodium hydroxide solution to produce a 150 mM solution at pH 14. Given the phenol side chain pK_a of 10.07,[49] we expect >99.9% deprotonation of the phenolic OH at pH 14. That is, tyrosine exists in our experiments in the dianionic form (Tyr^{2-}).

Theoretical calculations

The calculated equilibrium geometries and vibrational frequencies of tyrosinate dianion and tyrosyl radical anion are obtained with the GAUSSIAN 16 program.[50] The DFT calculations use the hybrid exchange functional of Becke (B3)[51] and the correlation functional of Lee, Yang and Parr (LYP),[52] and the 6-311G++(d,p) split-valence triple-zeta basis set. This basis set is augmented with d-orbital and diffuse functions on the heavy atoms (carbon, nitrogen and oxygen) and p-orbital and diffuse functions on the hydrogen atoms. Two models of the tyrosinate dianion and the tyrosyl radical anion are constructed. The first model is the isolated tyrosinate dianion and tyrosyl radical anion, while the second model is the microhydrated species. The microhydrated species includes three water molecules directly hydrogen-bonded to the oxygen atom of the phenolic sidechain. Furthermore, for both the isolated and microhydrated species, a polarizable continuum is included to mimic the interaction of the microhydrated species with the surrounding solvent.[53] The water molecules present in the microhydrated species are fully relaxed during geometry optimization. Each geometry optimization is followed by a vibrational frequency calculation to verify that the optimized geometry corresponds to a local minimum.

Results and discussion

Transient absorption of the aqueous tyrosyl radical anion

The differential absorption (ΔA) spectrum recorded as a function of pump–probe time delay, following the photodetachment of the aqueous tyrosinate dianion, is shown in Fig. 2. Strong-field-induced multiphoton photodetachment of tyrosinate dianion yields the tyrosyl radical anion (Tyr$^{\bullet-}$) and the hydrated electron. Tyr$^{\bullet-}$ has an absorption band peaking at 413 nm and a vibronic transition at 400 nm, consistent with previous studies of the tyrosyl radical in aqueous solution.[22,44,45] In addition, the increase in the ΔA signal at longer wavelengths beyond 430 nm is due to the absorption of the ground-state hydrated electron, which spans 300–1000 nm.[46]

Previous studies have shown that 4.68 eV (265 nm) photoexcitation of tyrosine to the S_1 ($\pi\pi^*$) state yields the tyrosyl radical *via* a two-photon process involving the lowest-energy triplet state of tyrosine as an intermediate.[22] In the present study, however, we discount the possibility that the tyrosyl radical anion is formed *via* the electronically excited states of the tyrosinate dianion. This is evident from the pump-power dependence measurements, which show the photodetachment occurs directly *via* a three-photon process (Fig. 3 and Section S1, ESI†). While the vertical ionization energy of the tyrosinate dianion is unknown, we note that tyrosine and phenol have identical vertical ionization energies of 7.8 eV.[6] As such, we expect the vertical ionization energies of the tyrosinate dianion and phenoxide to be similar; the latter is reported to be 7.1 eV,[37] with the photoelectron band extending to <6 eV binding energy. Considering that the bottom of the conduction band of liquid water resides ~1 eV below the vacuum level,[54] the total energy input of 5.9 eV that is associated with a three-photon photodetachment process is sufficient to remove an

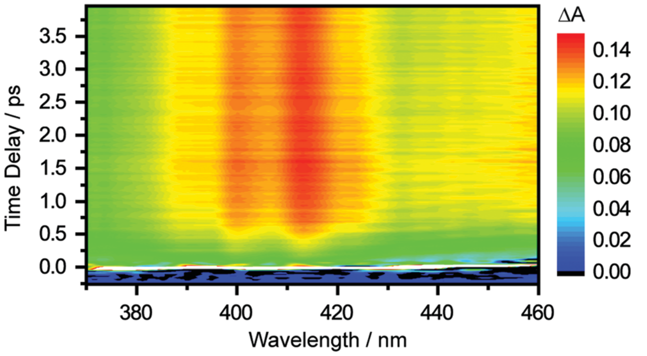

Fig. 2 Time-resolved differential absorption spectrum of the photodetached aqueous tyrosinate dianion as a function of pump–probe time delay.

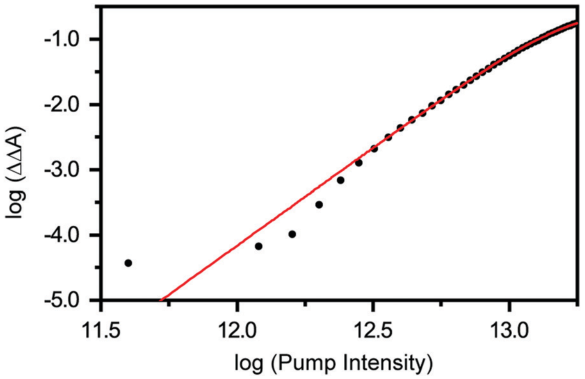

Fig. 3 Photon-order measurement for the strong-field photodetachment of the tyrosinate dianion. Log–log plot of $\Delta\Delta A$ *vs.* pump intensity after subtraction of the response from aqueous sodium hydroxide. The solid line is a fit to a three-photon photodetachment process.

electron from the tyrosinate dianion and inject it into the conduction band of liquid water.

Global fitting of the time-resolved ΔA spectra over the 370–455 nm probe wavelength range and 120 fs after time-zero to the function:

$$\Delta A(\lambda,t) = \Delta A_0(\lambda) + \Delta A_1(\lambda)(e^{-t/\tau_{d1}} - e^{-t/\tau_{r1}}) + \Delta A_2(\lambda)(e^{-t/\tau_{d2}}) - 1, \quad (1)$$

where $\Delta A_0(\lambda)$, $\Delta A_1(\lambda)$ and $\Delta A_2(\lambda)$ are spectral amplitudes, τ_{r1} and τ_{d1} reflect the time constants associated with the rise and decay of the hydrated electron population, respectively, and τ_{d2} is an additional decay component. To avoid contributions from coherent artifacts, the global fitting does not include the vicinity of time-zero. For the photodetachment of a pH 14 NaOH-only aqueous solution, we obtain τ_{r1} = 0.42 ± 0.01 ps and τ_{d1} = 54 ± 1 ps.

The formation and subsequent decay of the hydrated electron is modeled by sequential first-order kinetics (see the second term in eqn (1)). Hydrated electron formation involves the trapping of the electron that is initially injected into the conduction band by photodetachment[55] followed by vibrational cooling; this entire process can be modeled by first-order kinetics.[29–35] Since the hydrated electron depopulation occurs *via* geminate recombination, a process that exhibits nonexponential decay behavior,[29,56] the exponential decay constant that is extracted from our analysis should be regarded as merely an approximation to the decay of the hydrated electron population by geminate recombination and observed within a very narrow (<4 ps) time-delay window. Moreover, in view of an earlier finding that electron–ion recombination dynamics involving solutes in aqueous solution is considerably slower than the diffusion limit,[57] which suggests negligible recombination between tyrosyl radical anions and hydrated electrons on the few-picosecond timescale in our experiments, we employ the same time constants as those obtained from aqueous NaOH in our analysis. While a detailed analysis of the geminate recombination dynamics lies beyond the scope of the present work, a future study that varies the concentration of the Tyr^{2-} dianion solute and extends the pump–probe measurements to >0.1 ns time delays would allow one to disentangle the relative contributions of the geminate recombination channels that involve the hydroxyl radicals and the tyrosyl radical anions.

Extrapolating the $\Delta A(\lambda,t)$ time traces (Fig. 4(a)) collected for the photodetached tyrosinate dianion to time zero reveals an offset $\Delta A_0(\lambda)$, which indicates the formation of the tyrosyl

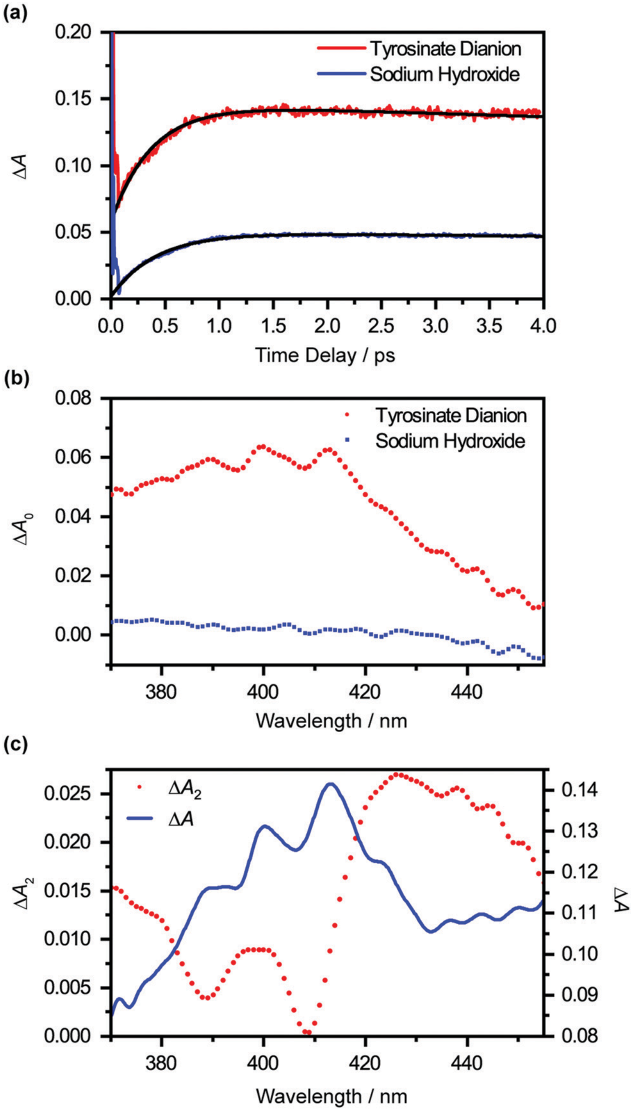

Fig. 4 (a) Time-traces at 413 nm of the photodetached aqueous tyrosinate dianion (red) and photodetached aqueous sodium hydroxide (blue). Note the offset that is present in the photodetached aqueous tyrosinate dianion time trace, which indicates the immediate formation of tyrosyl radical upon photodetachment. In addition, global fit analysis on both time-traces from 120 fs is performed, where the best-fit line is shown in black. (b) The wavelength-dependent offset values, ΔA_0, obtained from the global fitting of photodetached aqueous sodium hydroxide (blue) and photodetached aqueous tyrosinate dianion (red) time traces. The fitting errors are comparable to the size of the symbol. (c) The $\Delta A_2(\lambda)$ spectrum obtained from global fitting (red) and the ΔA spectrum of photodetached aqueous tyrosinate dianion at 2 ps time delay (blue).

radical anion immediately upon strong-field photodetachment (Fig. 4(b), in red). This offset is noticeably smaller for the time traces for photodetached aqueous sodium hydroxide obtained under similar experimental conditions (Fig. 4(b), in blue), consistent with the fact that the hydroxyl radical, produced by the photodetachment of aqueous hydroxide, does not exhibit any appreciable absorption in the >400 nm region ($\varepsilon_{\mathrm{OH}}$ = 30 M^{-1} cm^{-1} at 400 nm).[58] The wavelength-dependent offset $\Delta A_0(\lambda)$ that is obtained for the tyrosinate dianion corresponds to the absorption spectrum of the tyrosyl radical anion at the Franck–Condon region, generated immediately upon photodetachment, prior to vibrational cooling. Compared to the differential absorption spectra for the tyrosyl radical reported in the literature,[22,44,45] the additional broadening of $\Delta A_0(\lambda)$ towards the long-wavelength side is suggestive of a vibrationally excited tyrosyl radical anion that is produced immediately upon photodetachment. On the other hand, $\Delta A_0(\lambda)$ of the sodium hydroxide sample shows a gradual increase with decreasing probe wavelength, following the absorption spectral signature of the hydroxyl radical.[58]

Global analysis using eqn (1) gives $\tau_{\mathrm{d2}} = 0.93 \pm 0.02$ ps. Based on previous experimental results that reveal the stability of tyrosyl radical with respect to dissociation,[59] we exclude the possibility that the decay of the ΔA signal arises from photofragmentation. The appearance of the decay associated spectrum $\Delta A_2(\lambda)$ is suggestive of the decay of the ΔA signal in the long-wavelength region ($\lambda > 420$ nm) and the sharpening of the 400 nm and 413 nm absorption maxima of the $\mathrm{Tyr}^{\bullet -}$ radical spectrum. As such, we ascribe τ_{d2} to vibrational relaxation. A similar analysis performed on photodetached phenoxide anions in aqueous solution yields a vibrational relaxation timescale of 1.02 ± 0.03 ps,[36] suggesting that the amino acid backbone induces a small but noticeable increase in the vibrational relaxation. Due to the limited range of time delays ($\sim$4 ps) sampled in our experiments, however, we cannot rule out the possible existence of slower vibrational relaxation pathways.

Since $\Delta A_1(\lambda)$ tracks the formation of the hydrated electron and its subsequent decay by geminate recombination, it should follow the absorption spectrum of the hydrated electron. Using the relation:

$$\Delta A_1(\lambda) = \varepsilon_{\mathrm{e}}(\lambda) c_{\mathrm{e}} L, \tag{2}$$

where $\varepsilon_{\mathrm{e}}(\lambda)$ is the molar absorption coefficient of the hydrated electron,[58] c_{e} is the initial concentration of hydrated electrons produced by strong-field photodetachment of both the tyrosinate dianion and the hydroxide anion, and $L = 7 \pm 1$ μm is the sample path length, we obtain $c_{\mathrm{e}} = 44 \pm 6$ mM (Section S2 and Fig. S3, ESI†). To obtain an estimate of the concentration of the $\mathrm{Tyr}^{\bullet -}$ anion, we employ the relation

$$\Delta A_0(\lambda) = [\varepsilon_{\mathrm{Tyr}}(\lambda) c_{\mathrm{Tyr}} + \varepsilon_{\mathrm{OH}}(\lambda) c_{\mathrm{OH}}] L, \tag{3}$$

where $\varepsilon_{\mathrm{Tyr}}$ ($\varepsilon_{\mathrm{OH}}$) and c_{Tyr} (c_{OH}) are the molar absorption coefficients and initial concentrations of the vibrationally hot tyrosyl radical anion (vibrationally hot hydroxyl radical), respectively. Note that, since the hydrated electrons originate from the photodetachment of both Tyr^{2-} and OH^-, $c_{\mathrm{e}} = c_{\mathrm{Tyr}} + c_{\mathrm{OH}}$. In the absence of the molar absorption coefficients of the vibrationally hot species, we employ the molar absorption coefficients of the vibrationally relaxed species at 410 nm, reported in the literature ($\varepsilon_{\mathrm{Tyr}} = 2750$ M^{-1} cm^{-1} and $\varepsilon_{\mathrm{OH}} = 23$ M^{-1} cm^{-1}),[58,60] to obtain $c_{\mathrm{Tyr}} = 30 \pm 10$ mM and $c_{\mathrm{OH}} = 14 \pm 8$ mM. This result suggests that, under our experimental conditions, the photodetachment of Tyr^{2-} dominates over that of OH^-, and the photodetachment yield of Tyr^{2-} is $\sim$20%.

Vibrational wave packet dynamics

The time-resolved ΔA spectra (Fig. 2) reveal amplitude modulations as a function of time delay, suggesting the presence of vibrational wave packet dynamics. We exclude contributions from impulsive stimulated Raman scattering (ISRS) of the tyrosinate dianion to the observed wave packet dynamics because the absorption spectrum of the aqueous tyrosinate dianion (Fig. S4, ESI†) does not lie within the range of the probe spectrum. Moreover, the ΔA signal vanishes when the pump power is attenuated to suppress strong-field photodetachment.

To analyze the vibrational wave packet dynamics quantitatively, we compute the spectral first-moment $\langle E(t)\rangle$ time trace, given as

$$\langle E(t)\rangle = \frac{\int_{E_i}^{E_\mathrm{f}} E \Delta A(E,t) \mathrm{d}E}{\int_{E_i}^{E_\mathrm{f}} \Delta A(E,t) \mathrm{d}E}. \tag{4}$$

In the above expression, E represents the probe photon energy, t is the pump–probe time delay and $\Delta A(E,t)$ is the differential absorbance as a function of probe photon energy and pump–probe time delay. E_i and E_f define the spectral range that is used to compute the spectral first-moment; in this case, E_i and E_f correspond to 2.83 eV (438 nm) and 3.17 eV (391 nm), respectively. The resultant $\langle E(t)\rangle$, after removing the slow population dynamics, is shown in Fig. 5(a); a zoomed-in view of $\langle E(t)\rangle$ is shown in the inset of Fig. 5(a).

The oscillatory nature of the spectral first-moment time trace arises from vibrational wave packet motion of the tyrosyl radical anion. Wave packet motion along the vibrational mode Q_i requires photodetachment to project the vibrational probability density of Tyr^{2-} vertically onto the potential energy curve of $\mathrm{Tyr}^{\bullet -}$, and for the potential energy surfaces of Tyr^{2-} and $\mathrm{Tyr}^{\bullet -}$ to be displaced along Q_i. From the Franck–Condon region of the $\mathrm{Tyr}^{\bullet -}$ potential, temporal evolution of the coherent superposition of vibrational eigenstates leads to vibrational wave packet motion. This wave packet motion in turn modulates the probe transition energy of the $\mathrm{Tyr}^{\bullet -}$ anion radical, giving rise to the observed oscillations in the first-moment time trace. It is important to note that vibrational wave packet motion can be initiated by such a displacive mechanism only when the equilibrium geometries of Tyr^{2-} and $\mathrm{Tyr}^{\bullet -}$ are displaced along a given vibrational mode Q_i. The vibrational modes can be identified by their characteristic frequencies, in turn obtained from the fast-Fourier transform (FFT) power spectrum of the first-moment time trace (Fig. 5(b), in red).

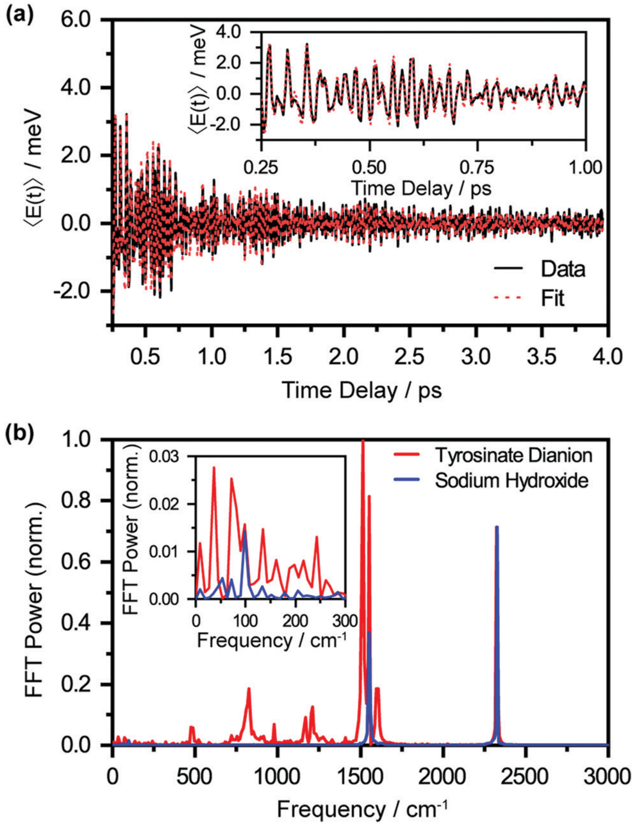

Fig. 5 (a) First-moment time-trace ⟨*E*(*t*)⟩ of photodetached aqueous tyrosinate dianion with fit function. The inset shows the enlarged first-moment time-trace ⟨*E*(*t*)⟩ from 0.25 ps to 1 ps. (b) FFT power spectra of the first-moment time trace of photodetached aqueous tyrosinate anion (in red) and photodetached aqueous sodium hydroxide (in blue). The peaks observed are vibrational frequencies associated with the tyrosyl radical anion. Note that the oxygen and nitrogen vibrational frequencies are also observed at 1554 cm^{-1} and 2328 cm^{-1}, respectively. The inset shows the enlarged FFT power spectrum from 0 to 300 cm^{-1}.

These frequencies and their relative FFT powers are summarized in Table 1.

A control experiment performed with aqueous NaOH (pH 14) under similar photodetachment conditions confirms that the oscillatory features observed in the first-moment time trace originate from photodetached tyrosinate dianion. The FFT power spectrum of photodetached aqueous NaOH is shown in Fig. 5(b), in blue. Here, the only observed frequencies are 1554 cm^{-1} and 2328 cm^{-1}, which correspond to the stretching frequencies of oxygen (O_2) and nitrogen (N_2), respectively.[61,62] These frequencies, also present in the FFT power spectrum of the photodetached tyrosinate dianion, are due to ISRS of N_2 and O_2, which in turn arise from the experiments being performed in air. The estimated vibrational frequency of the OH$^{\bullet}$ radical, produced by photodetachment of OH^{-}, is ~3880 cm^{-1},[63] beyond the high-frequency cut-off of our experiment. Based on the results of the control experiment, we conclude that the remaining seven vibrational frequencies reported in Table 1 are associated with the tyrosyl radical anion.[64,65]

Aside from FFT, the first-moment time-trace can also be analyzed in the time domain by fitting it to a sum of exponentially damped cosine functions,

$$\langle E(t)\rangle = \sum_{i=1}^{n} A_i \mathrm{e}^{-t/\tau_i}\cos(\omega_i t + \phi_i). \qquad (5)$$

In the above expression, A_i, τ_i, ω_i, and ϕ_i are the respective amplitude, dephasing time, vibrational frequency, and phase of the vibrational mode Q_i. The fit parameters are summarized in Table 1. Compared to FFT, time-domain analysis directly furnishes the dephasing times of the vibrational modes. The majority of the vibrational modes have dephasing times on the order of ~1 ps, comparable to those observed for other molecules in the condensed phase.[66,67] The vibrational modes at 816 and 1000 cm^{-1}, however, exhibit markedly shorter dephasing times of ~0.2 ps.

It is interesting to compare the photodetachment-induced vibrational wave packet dynamics of the tyrosyl radical anion and the phenoxyl radical. The vibrational wave packet dynamics triggered by the photodetachment of aqueous phenoxide is characterized by an FFT power spectrum that is strongly peaked at 527 cm^{-1}. This vibrational frequency, assigned to the benzene CCC bend, also dominates the Franck–Condon

Table 1 Experimental FFT power, time-domain analysis results, and calculated vibrational frequencies of the tyrosyl radical anion in aqueous solution and their assignments. The calculated frequencies are based on the equilibrium geometry of the microhydrated tyrosyl radical anion. Numbered assignments denote benzene ring modes in the Wilson notation[62,63]

Experimental							
FFT Analysis		Time-domain analysis					
Frequency (cm^{-1})	Power (norm.)	Frequency (cm^{-1})	Amplitude (meV)	Dephasing Time (ps)	Phase (π rad)	Calculated frequency (cm^{-1})	Assignment
476	6.0×10^{-2}	483 ± 1	0.45 ± 0.06	0.90 ± 0.14	1.06 ± 0.04	482	6a
825	1.9×10^{-1}	816 ± 2	7.29 ± 0.84	0.19 ± 0.01	0.77 ± 0.04	832	1
978	6.8×10^{-2}	1000 ± 3	2.19 ± 0.46	0.25 ± 0.03	0.74 ± 0.07	994	19a
1166	9.1×10^{-2}	1172 ± 1	0.41 ± 0.06	1.30 ± 0.37	0.54 ± 0.06	1185	8a
1211	1.3×10^{-1}	1210 ± 1	1.03 ± 0.13	0.65 ± 0.10	0.30 ± 0.05	1240	13
1516	1	1515 ± 1	2.01 ± 0.09	0.77 ± 0.06	1.69 ± 0.02	1520	20a
1606	1.9×10^{-1}	1601 ± 1	1.11 ± 0.09	0.73 ± 0.10	0.60 ± 0.03	1626	9a
1552	8.1×10^{-1}	1554 ± 1	0.40 ± 0.03	3.67 ± 0.55	0.45 ± 0.01		O_2
2324	7.1×10^{-1}	2328 ± 1	0.47 ± 0.03	4.01 ± 0.45	0.56 ± 0.01		N_2

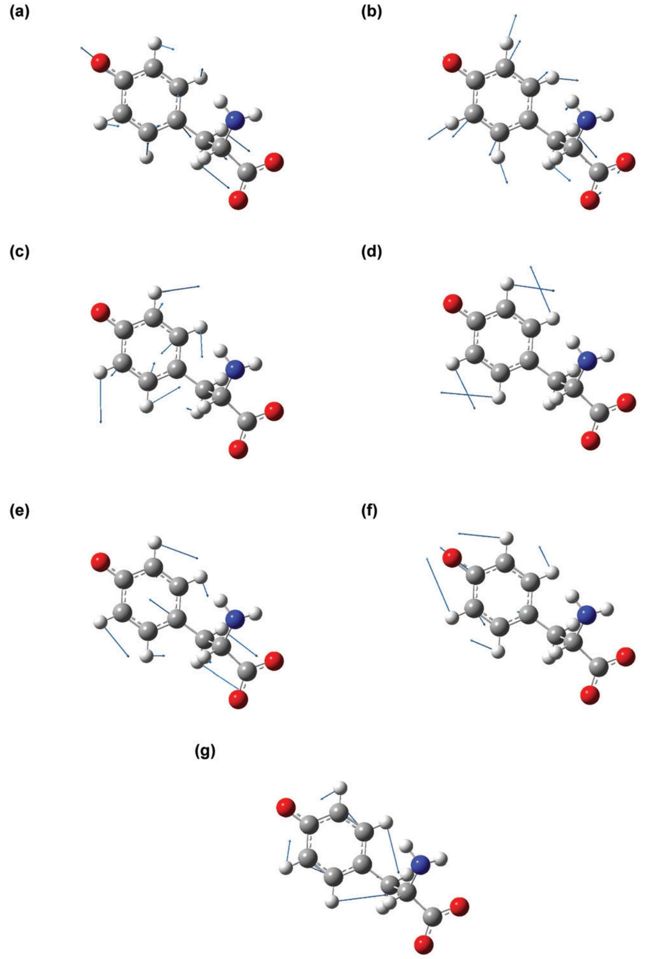

Fig. 6 Vibrational modes of tyrosyl radical anion coupled to the photodetachment, corresponding to the calculated frequencies (a) 482 cm^{-1} (b) 832 cm^{-1} (c) 994 cm^{-1} (d) 1185 cm^{-1} (e) 1240 cm^{-1} (f) 1520 cm^{-1} (g) 1626 cm^{-1}. The blue arrows indicate the direction and magnitude of the displacement of the atoms.

progression observed in the gas-phase photodetachment spectrum of phenoxide.[68] On the other hand, the largest FFT power observed in the photodetachment-induced vibrational coherence of the tyrosyl radical anion is associated with the C–O stretch at 1515 cm^{-1} (Fig. 5(b), in red); in comparison, the FFT power of the corresponding CCC bending mode in the tyrosyl radical anion, downshifted to 483 cm^{-1}, is $>10\times$ weaker. Aside from changes in the relative FFT power, the vibrational modes at 816 and 1000 cm^{-1} of the tyrosyl radical anion also exhibit dephasing times that are $\sim 3\times$ shorter than those of the corresponding modes of the phenoxyl radical. This faster dephasing is suggestive of anharmonic coupling of these benzene ring modes to the amino acid backbone of tyrosine, a subject for future investigations.

Theoretical calculations

The vibrational modes that contribute to the vibrational wave packet signal are assigned with the aid of *ab initio* vibrational frequency calculations. The calculated vibrational frequencies reported in Table 1 are those of the microhydrated model; the assignments should be considered tentative due to the presence of multiple calculated vibrational frequencies in the vicinity of each of the experimentally observed frequency. Although including explicit water molecules of solvation does not shift the vibrational frequencies that are higher than 200 cm^{-1} appreciably ($\sim$1% or less), their presence is necessary to model the intermolecular vibrational modes involved in the solvation of the tyrosyl radical anion. The complete list of vibrational frequencies of the tyrosyl radical anion, along with their assignments, are tabulated in the Supplementary Information (Table S1, ESI†).

The displacement vectors of the vibrational modes that contribute to the first-moment time trace are largely localized on the phenoxide moiety (Fig. 6). This result can be rationalized by considering the electronic character of the orbital from which the electron is ejected. Strong-field processes preferentially eject the most weakly bound electrons from molecules. Within a molecular orbital picture, this implies that the electron that lies in the highest occupied molecular orbital (HOMO) of the tyrosinate dianion has the highest probability of being removed by strong-field photodetachment. The calculated HOMO is primarily localized on the phenoxide sidechain (Fig. 7). Removal of an electron from the HOMO therefore leads to vibrational wave packet motion encoding primarily the structural rearrangement of the phenoxide sidechain, as seen from the few-picometer changes in the calculated C–O and C–C bond lengths of microhydrated Tyr^{2-} and $Tyr^{\bullet -}$ (Table 2). In addition to the phenoxide moiety, the HOMO also bears a significant albeit minor contribution from the α and β carbon atoms, which explains the calculated changes in the C–C bond distances involving the amino acid backbone; the C–C stretching character is present in the vibrational modes with

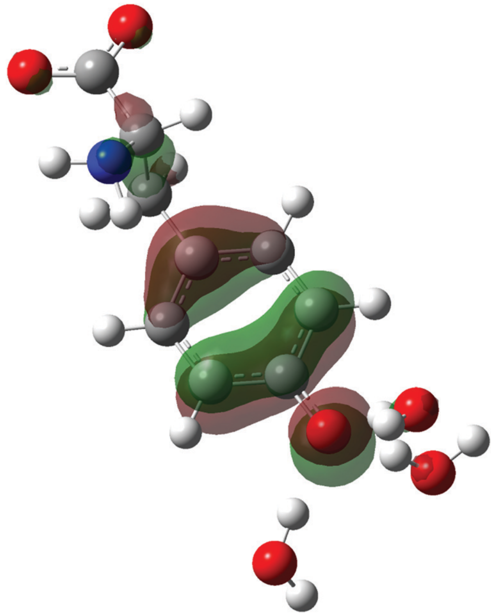

Fig. 7 Highest occupied molecular orbital (HOMO) of the microhydrated tyrosinate dianion.

Table 2 Results of DFT calculations, showing selected bond lengths of the tyrosinate dianion and the tyrosyl radical anion, and the difference bond lengths in aqueous solution and bond lengths of phenoxide and phenoxyl radical from a previous study[36]

	Bond length/pm			Bond length/pm		
Bond	Tyrosinate dianion	Tyrosyl radical anion	Difference/pm	Phenoxide anion	Phenoxyl radical	Difference/pm
C1–C2	155.2	156.3	1.1			
C2–C3	155.7	158.8	3.1			
C3–C4	151.2	148.5	−2.7			
C4–C5	140.1	141.9	1.8	141.7	144.8	3.1
C5–C6	139.5	137.1	−2.4	139.3	137.2	−2.1
C6–C7	141.3	144.4	3.1	139.8	141.1	1.3
C7–C8	141.7	144.5	2.8	139.8	141.1	1.3
C8–C9	139.1	136.8	−2.3	139.3	137.2	−2.1
C9–C4	140.3	142.3	2.0	141.7	144.8	3.1
C7–O10	132.9	127.3	−5.6	132.6	126.8	−5.8
O10–O23	269.8	289.0	19.2			
O10–O24	269.7	289.0	19.3			
O10–O25	268.9	283.8	14.9			

frequencies 832, 1240, and 1626 cm^{-1}. While the change in the C–O bond length is comparable to that calculated at the same level of theory for the photodetachment of phenoxide,[36] and changes in the C–C bond lengths differ from those calculated for phenoxide, suggesting that the amino acid backbone influences the relative contributions of the various vibrational modes to the structural reorganization. This result in turn provides a possible explanation for the qualitatively different appearance of the FFT power spectra associated with vibrational wave packet motion of the phenoxyl radical[36] and the tyrosyl radical anion (Fig. 5(b)).

Structural changes that are induced by photodetachment are not confined to the covalent framework of the amino acid itself. According to the DFT calculations, the intermolecular O···O distance increases from 2.69–2.70 Å in the microhydrated tyrosinate dianion to 2.84–2.89 Å in the microhydrated tyrosyl radical anion. These O···O distances lie within the range of 2.7–3.0 Å that is characteristic of hydrogen bonding.[69,70] The increase in the intermolecular O···O distances can be attributed to the weakening of the hydrogen bond caused by the removal of electron density on the phenoxide oxygen. The large changes in the intermolecular distance upon photodetachment should trigger coherent hindered translational motion, typically overdamped in liquid water.[71,72] Our DFT calculations predict that these intermolecular motions are characterized by vibrational frequencies of ∼130–160 cm^{-1} (Table S2, ESI†), coinciding with a band observed in the low-frequency region of the FFT power spectrum (Fig. 5(b), inset). Future investigations will aim to elucidate the ultrafast solvation dynamics that accompany the photodetachment process.

Conclusions

In conclusion, femtosecond strong-field photodetachment of the tyrosinate dianion in aqueous solution results in vibrational wave packet dynamics of the tyrosyl radical anion product. The wave packet motion is resolved into seven different vibrational modes and assigned with the aid of DFT calculations. These vibrational modes are observed because they participate in ultrafast structural reorganization upon photodetachment, consistent with their displacement vectors being largely localized on the phenoxide side chain, from which the electron is photodetached. Compared to previous experimental results for the aqueous phenoxyl radical, prepared by the strong-field photodetachment of aqueous phenoxide, we find that the presence of the amino acid backbone in the tyrosine radical anion changes the relative FFT intensities and decreases the dephasing times of certain vibrational modes. Moreover, the DFT calculations of the microhydrated tyrosinate dianion and the tyrosine radical anion suggests that photodetachment is accompanied by the elongation of the hydrogen-bonded O···O distances by ∼0.2 Å. Solvation dynamics driven by photoionization or photodetachment will be a subject of future investigations. The observation of these photodetachment-induced vibrational coherences of the tyrosyl radical anion in aqueous solution offers a glimpse into the elementary structural dynamics that accompany the interaction of ionizing radiation with biological molecules. These results suggest that our experimental approach can be extended to other redox-active amino acids such as tryptophan and phenylalanine as well as to larger biomolecules.

Conflicts of interest

There are no conflicts of interest to declare.

Acknowledgements

We acknowledge financial support from the Ministry of Education, Singapore (RG1/20, RG105/17, and MOE2014-T2-2-052). M. S. B. M. Y. is supported by the Nanyang President's Graduate Scholarship.

References

1 E. J. Hart, *Annu. Rev. Nucl. Sci.*, 1965, **15**, 125–150.

2 B. C. Garrett, D. A. Dixon, D. M. Camaioni, D. M. Chipman, M. A. Johnson, C. D. Jonah, G. A. Kimmel, J. H. Miller, T. N. Rescigno, P. J. Rossky, S. S. Xantheas, S. D. Colson, A. H. Laufer, D. Ray, P. F. Barbara, D. M. Bartels, K. H. Becker, K. H. Bowen, S. E. Bradforth, I. Carmichael, J. V. Coe, L. R. Corrales, J. P. Cowin, M. Dupuis, K. B. Eisenthal, J. A. Franz, M. S. Gutowski, K. D. Jordan, B. D. Kay, J. A. LaVerne, S. V. Lymar, T. E. Madey, C. W. McCurdy, D. Meisel, S. Mukamel, A. R. Nilsson, T. M. Orlando, N. G. Petrik, S. M. Pimblott, J. R. Rustad, G. K. Schenter, S. J. Singer, A. Tokmakoff, L.-S. Wang and T. S. Zwier, *Chem. Rev.*, 2005, **105**, 355–390.

3 P. Wardman, *Br. J. Radiol.*, 2009, **82**, 89–104.

4 P. H. Cannington and N. S. Ham, *J. Electron Spectrosc. Relat. Phenom.*, 1983, **32**, 139–151.

5 D. M. Close, *J. Phys. Chem. A*, 2011, **115**, 2900–2912.

6 A. Roy, R. Seidel, G. Kumar and S. E. Bradforth, *J. Phys. Chem. B*, 2018, **122**, 3723–3733.

7 B. M. K. Gmeiner and C. C. C. Seelos, *Free Radical Biol. Med.*, 1996, **21**, 349–351.

8 C. Grangeasse, A. J. Cozzone, J. Deutscher and I. Mijakovic, *Trends Biochem. Sci.*, 2007, **32**, 86–94.

9 T. Hunter, *Curr. Opin. Cell Biol.*, 2009, **21**, 140–146.

10 L. J. Getz, C. S. Runte, J. K. Rainey and N. A. Thomas, *J. Bacteriol.*, 2019, **201**, e00205–00219.

11 O. B. Morozova, A. S. Kiryutin, R. Z. Sagdeev and A. V. Yurkovskaya, *J. Phys. Chem. B*, 2007, **111**, 7439–7448.

12 J. J. Warren, J. R. Winkler and H. B. Gray, *FEBS Lett.*, 2012, **586**, 596–602.

13 D. R. Weinberg, C. J. Gagliardi, J. F. Hull, C. F. Murphy, C. A. Kent, B. C. Westlake, A. Paul, D. H. Ess, D. G. McCafferty and T. J. Meyer, *Chem. Rev.*, 2012, **112**, 4016–4093.

14 T. G. McCaslin, C. V. Pagba, H. Hwang, J. C. Gumbart, S.-H. Chi, J. W. Perry and B. A. Barry, *Chem. Commun.*, 2019, **55**, 9399–9402.

15 F. Lacombat, A. Espagne, N. Dozova, P. Plaza, P. Müller, K. Brettel, S. Franz-Badur and L.-O. Essen, *J. Am. Chem. Soc.*, 2019, **141**, 13394–13409.

16 J. Stubbe, D. G. Nocera, C. S. Yee and M. C. Y. Chang, *Chem. Rev.*, 2003, **103**, 2167–2202.

17 S. Hammes-Schiffer, *Energy Environ. Sci.*, 2012, **5**, 7696–7703.

18 A. Migliore, N. F. Polizzi, M. J. Therien and D. N. Beratan, *Chem. Rev.*, 2014, **114**, 3381–3465.

19 S. Hammes-Schiffer, *J. Am. Chem. Soc.*, 2015, **137**, 8860–8871.

20 J. Feitelson and E. Hayon, *J. Phys. Chem.*, 1973, **77**, 10–15.

21 J. Feitelson, E. Hayon and A. Treinin, *J. Am. Chem. Soc.*, 1973, **95**, 1025–1029.

22 D. V. Bent and E. Hayon, *J. Am. Chem. Soc.*, 1975, **97**, 2599–2606.

23 C. R. Johnson, M. Ludwig and S. A. Asher, *J. Am. Chem. Soc.*, 1986, **108**, 905–912.

24 I. Ayala, K. Range, D. York and B. A. Barry, *J. Am. Chem. Soc.*, 2002, **124**, 5496–5505.

25 H. F. Hameka and J. O. Jensen, *Comput. Theor. Chem.*, 1993, **288**, 9–16.

26 B. A. Barry, J. Chen, J. Keough, D. Jenson, A. Offenbacher and C. Pagba, *J. Phys. Chem. Lett.*, 2012, **3**, 543–554.

27 C. V. Pagba, T. G. McCaslin, G. Veglia, F. Porcelli, J. Yohannan, Z. Guo, M. McDaniel and B. A. Barry, *Nat. Commun.*, 2015, **6**, 10010.

28 K. Pirisi, L. Nag, Z. Fekete, J. N. Iuliano, J. Tolentino Collado, I. P. Clark, I. Pécsi, P. Sournia, U. Liebl, G. M. Greetham, P. J. Tonge, S. R. Meech, M. H. Vos and A. Lukacs, *Photochem. Photobiol. Sci.*, 2021, **20**, 369–378.

29 R. A. Crowell and D. M. Bartels, *J. Phys. Chem.*, 1996, **100**, 17940–17949.

30 C. Pépin, T. Goulet, D. Houde and J. P. Jay-Gerin, *J. Phys. Chem. A*, 1997, **101**, 4351–4360.

31 C. Silva, P. K. Walhout, K. Yokoyama and P. F. Barbara, *Phys. Rev. Lett.*, 1998, **80**, 1086–1089.

32 V. H. Vilchiz, J. A. Kloepfer, A. C. Germaine, V. A. Lenchenkov and S. E. Bradforth, *J. Phys. Chem. A*, 2001, **105**, 1711–1723.

33 M. S. Pshenichnikov, A. Baltuška and D. A. Wiersma, *Chem. Phys. Lett.*, 2004, **389**, 171–175.

34 M. Mostafavi and I. Lampre, *Recent Trends in Radiation Chemistry*, 2010, pp. 21–58, DOI: 10.1142/9789814282093_0002.

35 M. H. Elkins, H. L. Williams, A. T. Shreve and D. M. Neumark, *Science*, 2013, **342**, 1496–1499.

36 T. Debnath, M. S. B. Mohd Yusof, P. J. Low and Z.-H. Loh, *Nat. Commun.*, 2019, **10**, 2944.

37 D. Ghosh, A. Roy, R. Seidel, B. Winter, S. Bradforth and A. I. Krylov, *J. Phys. Chem. B*, 2012, **116**, 7269–7280.

38 B. Winter, R. Weber, W. Widdra, M. Dittmar, M. Faubel and I. V. Hertel, *J. Phys. Chem. A*, 2004, **108**, 2625–2632.

39 K. Nishizawa, N. Kurahashi, K. Sekiguchi, T. Mizuno, Y. Ogi, T. Horio, M. Oura, N. Kosugi and T. Suzuki, *Phys. Chem. Chem. Phys.*, 2011, **13**, 413–417.

40 N. Kurahashi, S. Karashima, Y. Tang, T. Horio, B. Abulimiti, Y.-I. Suzuki, Y. Ogi, M. Oura and T. Suzuki, *J. Chem. Phys.*, 2014, **140**, 174506.

41 C. F. Perry, P. Zhang, F. B. Nunes, I. Jordan, A. von Conta and H. J. Wörner, *J. Phys. Chem. Lett.*, 2020, **11**, 1789–1794.

42 B. Winter, M. Faubel, R. Vácha and P. Jungwirth, *Chem. Phys. Lett.*, 2009, **474**, 241–247.

43 R. Carta and G. Tola, *J. Chem. Eng. Data*, 1996, **41**, 414–417.

44 A. Gräslund, M. Sahlin and B. M. Sjöberg, *Environ. Health Perspect.*, 1985, **64**, 139–149.

45 S. Oldemeyer, S. Franz, S. Wenzel, L.-O. Essen, M. Mittag and T. Kottke, *J. Biol. Chem.*, 2016, **291**, 14062–14071.

46 P. M. Hare, E. A. Price and D. M. Bartels, *J. Phys. Chem. A*, 2008, **112**, 6800–6802.

47 M. Dantus, V. Lozovoy and I. Pastirk, *Laser Focus World*, 2007, **43**, 101–104.

48 D. Pestov, V. V. Lozovoy and M. Dantus, *Opt. Express*, 2009, **17**, 14351–14361.

49 D. L. Nelson, M. M. Cox and A. L. Lehninger, *Principles of Biochemistry*, W.H. Freeman, New York, 7th edn, 2017.

50 M. J. Frisch, G. W. Trucks, H. B. Schlegel, G. E. Scuseria, M. A. Robb, J. R. Cheeseman, G. Scalmani, V. Barone, G. A. Petersson, H. Nakatsuji, X. Li, M. Caricato, A. V. Marenich, J. Bloino, B. G. Janesko, R. Gomperts,

B. Mennucci, H. P. Hratchian, J. V. Ortiz, A. F. Izmaylov, J. L. Sonnenberg, D. Williams-Young, F. Ding, F. Lipparini, F. Egidi, J. Goings, B. Peng, A. Petrone, T. Henderson, D. Ranasinghe, V. G. Zakrzewski, J. Gao, N. Rega, G. Zheng, W. Liang, M. Hada, M. Ehara, K. Toyota, R. Fukuda, J. Hasegawa, M. Ishida, T. Nakajima, Y. Honda, O. Kitao, H. Nakai, T. Vreven, K. Throssell, J. A. Montgomery Jr., J. E. Peralta, F. Ogliaro, M. J. Bearpark, J. J. Heyd, E. N. Brothers, K. N. Kudin, V. N. Staroverov, T. A. Keith, R. Kobayashi, J. Normand, K. Raghavachari, A. P. Rendell, J. C. Burant, S. S. Iyengar, J. Tomasi, M. Cossi, J. M. Millam, M. Klene, C. Adamo, R. Cammi, J. W. Ochterski, R. L. Martin, K. Morokuma, O. Farkas, J. B. Foresman and D. J. Fox, *Gaussian 16 Rev. C.01*, Gaussian Inc, Wallingford, CT, 2016.

51 A. D. Becke, *Phys. Rev. A: At., Mol., Opt. Phys.*, 1988, **38**, 3098–3100.

52 C. Lee, W. Yang and R. G. Parr, *Phys. Rev. B: Condens. Matter Mater. Phys.*, 1988, **37**, 785–789.

53 J. Tomasi, B. Mennucci and R. Cammi, *Chem. Rev.*, 2005, **105**, 2999–3094.

54 F. Ambrosio, Z. Guo and A. Pasquarello, *J. Phys. Chem. Lett.*, 2018, **9**, 3212–3216.

55 F. Ambrosio, G. Miceli and A. Pasquarello, *J. Phys. Chem. Lett.*, 2017, **8**, 2055–2059.

56 J. A. Kloepfer, V. H. Vilchiz, V. A. Lenchenkov, A. C. Germaine and S. E. Bradforth, *J. Chem. Phys.*, 2000, **113**, 6288–6307.

57 J. Peon, G. C. Hess, J.-M. L. Pecourt, T. Yuzawa and B. Kohler, *J. Phys. Chem. A*, 1999, **103**, 2460–2466.

58 G. Czapski and B. H. J. Bielski, *Radiat. Phys. Chem.*, 1993, **41**, 503–505.

59 J. A. Noble, J. P. Aranguren-Abate, C. Dedonder, C. Jouvet and G. A. Pino, *Phys. Chem. Chem. Phys.*, 2019, **21**, 23346–23354.

60 L. Petersson, A. Gräslund, A. Ehrenberg, B. M. Sjöberg and P. Reichard, *J. Biol. Chem.*, 1980, **255**, 6706–6712.

61 J. H. Odhner, D. A. Romanov and R. J. Levis, *Phys. Rev. Lett.*, 2009, **103**, 075005.

62 R. Salter, J. Chu and M. Hippler, *Analyst*, 2012, **137**, 4669–4676.

63 Z.-H. Loh, G. Doumy, C. Arnold, L. Kjellsson, S. H. Southworth, A. Al Haddad, Y. Kumagai, M.-F. Tu, P. J. Ho, A. M. March, R. D. Schaller, M. S. Bin Mohd Yusof, T. Debnath, M. Simon, R. Welsch, L. Inhester, K. Khalili, K. Nanda, A. I. Krylov, S. Moeller, G. Coslovich, J. Koralek, M. P. Minitti, W. F. Schlotter, J.-E. Rubensson, R. Santra and L. Young, *Science*, 2020, **367**, 179–182.

64 E. B. Wilson, *Phys. Rev.*, 1934, **45**, 706–714.

65 L. I. Grace, R. Cohen, T. M. Dunn, D. M. Lubman and M. S. de Vries, *J. Mol. Spectrosc.*, 2002, **215**, 204–219.

66 J. C. Dean, S. Rafiq, D. G. Oblinsky, E. Cassette, C. C. Jumper and G. D. Scholes, *J. Phys. Chem. A*, 2015, **119**, 9098–9108.

67 S. Rafiq and G. D. Scholes, *J. Phys. Chem. A*, 2016, **120**, 6792–6799.

68 J. B. Kim, T. I. Yacovitch, C. Hock and D. M. Neumark, *Phys. Chem. Chem. Phys.*, 2011, **13**, 17378–17383.

69 G. A. Jeffrey, *An Introduction to Hydrogen Bonding*, Oxford University Press, New York, 1997.

70 P. Gilli, L. Pretto, V. Bertolasi and G. Gilli, *Acc. Chem. Res.*, 2009, **42**, 33–44.

71 S. Palese, L. Schilling, R. J. D. Miller, P. R. Staver and W. T. Lotshaw, *J. Phys. Chem.*, 1994, **98**, 6308–6316.

72 C. J. Fecko, J. D. Eaves and A. Tokmakoff, *J. Chem. Phys.*, 2002, **117**, 1139–1154.